

1 **CHARACTERIZING DROPLET BREAKUP RATES OF SHEAR-THINNING**
2 **DISPERSED PHASE IN MICROREACTORS**

3 Voon-Loong Wong^{a,b,*,1}, Katerina Loizou^{b,2}, Phei-Li Lau^a, Richard S. Graham^c, and
4 Buddhika N. Hewakandamby^c

5
6 ^aDepartment of Chemical and Environmental Engineering, University of Nottingham
7 Malaysia Campus, Semenyih 43500, Malaysia

8 ^bDepartment of Chemical and Environmental Engineering, University of Nottingham,
9 Nottingham NG7 2RD, United Kingdom

10 ^cSchool of Mathematical Sciences, University of Nottingham, Nottingham NG7 2RD,
11 United Kingdom

12 **ABSTRACT**

13 A two-phase flow predictive model with the integration of conservative level-set
14 method (LSM) and Carreau-Yasuda constitutive equation was developed herein. The
15 LSM was chosen as a potential interface capturing scheme for elucidating the
16 interfacial phenomena including insight into the mechanism of shear-thinning droplets.
17 In present paper, the dynamics of shear-dependent droplet emergence, growth,
18 detachment and translocation in a Newtonian microsystem were examined via
19 computational fluid dynamics (CFD) analysis. Dilute sodium carboxymethylcellulose
20 (Na-CMC) solution was treated as dispersed phase ($70 \text{ mPa}\cdot\text{s} < \eta_o < 10.2644 \text{ Pa}\cdot\text{s}$)
21 whereas the olive oil ($68 \text{ mPa}\cdot\text{s}$) was designated as continuous phase. Visualisation
22 experiments were carried out and these laboratory data were used to validate the
23 simulation results. Detailed 2D simulations were presented to examine systematically
24 the impact of fluid properties on the droplet breakup rate at predefined flow rate ratio,
25 Q of 0.05. The results yielded an inflection point in the dependence of droplet breakup
26 rate on Na-CMC concentration was found in between the dilute and semi-dilute
27 concentration regimes. This inflection point displays a non-monotonic profile which is
28 mainly caused by the considerable viscosity effect of Na-CMC polymer when its
29 concentration increases above a critical value ($C > C^* \sim 0.40 \text{ wt}\%$). This striking

* Corresponding author; v.wong@hw.ac.uk (Voon-Loong Wong)

¹Current address: School of Engineering and Physical Sciences, Heriot-Watt University Malaysia Campus, 62200 Putrajaya Wilayah Persekutuan, Malaysia.

²Current address: Department of Chemical Engineering, University College London, London, United Kingdom.

30 behaviour highlights the importance of rheological effects in flows with a shear-
31 dependent fluid under various flow conditions. The viscous effect of Na-CMC fluids
32 substantially affects the manipulation over the droplet pinch-off time and production
33 rate. Thus, it necessitate the control of the shear rate by adjusting the flow conditions
34 and aspect ratio of microchannels.

35 **Keywords:** non-Newtonian; microfluidics; level-set; droplet breakup; T-junction
36 geometry.

37

38 **1. Introduction**

39 Two-phase flow is a term covering the motion of two different interacting fluids that are
40 in different phases such as liquid-liquid and liquid-vapor. In two-phase flow
41 microfluidics, an emulsion contains a mixture of two immiscible liquids as one phase
42 being dispersed throughout the other phase in small droplets. Most common
43 emulsions include direct emulsions, oil droplets in an immiscible and continuous water
44 phase, or inverted emulsions, water droplets in an immiscible and continuous oil
45 phase. Emulsions are typically made by fissioning droplets with shear or impact and
46 the resulting suspensions possess a wide size distribution of drop sizes (Umbanhowar,
47 Prasad, & Weitz, 2000). At low enough Reynolds (Re) number, a laminar flow regime
48 is assumed and these droplets are translocate through microfluidic structures having
49 dimensions most easily measured in microns. The manipulation of droplets in a
50 confined microfluidic system has been highlighted as one of the earliest tools used in
51 the fields of biomedical sciences. The characteristics of droplets become reliable tool
52 for performing biological operations such as analyte encapsulation, sampling,
53 metering, dilution, reaction and detection (Huebner et al., 2008; Niu & deMello, 2012;
54 Tawfik & Griffiths, 1998; Theberge Ashleigh et al., 2010).

55 Droplets can be generated via a number of methods in microfluidic devices, including
56 breakup in co-flowing stream(Cramer, Fischer, & Windhab, 2004; Moon, Cheong, &
57 Choi, 2014; Utada, Fernandez-Nieves, Stone, & Weitz, 2007), breakup in cross-
58 flowing stream (Garstecki, Fuerstman, Stone, & Whitesides, 2006; Qiu, Silva,
59 Tonkovich, & Arora, 2010; Xu, Li, Tan, & Luo, 2008), hydrodynamics flow-focusing
60 (Anna & Mayer, 2006; Peng, Yang, Guo, Liu, & Zhao, 2011), and microchannel

61 emulsification (Kobayashi, Nakajima, & Mukataka, 2003; van der Zwan, Schroën, &
62 Boom, 2009; Yobas, Martens, Ong, & Ranganathan, 2006). Cross-flowing in a T-
63 junction is one of the easiest microfluidic methods of generating highly monodispersed
64 droplets. The formation of droplet at a T-junction, at which viscous shear-stresses
65 induced by continuous stream of the horizontal channel overcome surface tension at
66 the liquid-liquid interface and pull off droplets of the dispersed phase from the vertical
67 channel. This is mainly due to the instabilities of free surface between the phases are
68 sufficiently large. Thus, the size and frequency of the droplets can be accurately
69 manipulated by modifying the relative pressures of the two immiscible liquid in order
70 to enable the production of a wide range of vesicle shapes and patterns (Thorsen,
71 Roberts, Arnold, & Quake, 2001). Besides, opposed flowing (Shui, van den Berg, &
72 Eijkel, 2009) and perpendicular flowing (Leshansky & Pismen, 2009) are another
73 operation modes producing monodispersed droplet formation in a T-junction
74 microchannel.

75 A numerical modelling approach to the multiphase flow problem provides a detailed
76 and comprehensive description of the formation of microdroplets since a number of
77 statistical information can be extracted from a predictive model. As the dimension of
78 the interest gets smaller, the surface-based interfacial tension and the viscosity
79 become more significant in controlling critical flow behavior of multiphase flow in
80 microscale, especially when handling fluids that have a complex microstructure
81 leading to non-Newtonian phenomena. Additionally, the non-Newtonian flow curve
82 presents a nonlinear relationship between shear-stress and the rate of deformation.
83 For instance, previous research efforts have been much devoted to the experimental
84 analysis of the dynamics and relevant hydrodynamics of viscoelastic droplets (Arratia,
85 Cramer, Gollub, & Durian, 2009; Husny & Cooper-White, 2006; Steinhaus, Shen, &
86 Sureshkumar, 2007) and few studies have focused on other shear-dependent fluids
87 such as purely viscous fluids and time-dependent fluids (Chhabra & Richardson,
88 2008). Hitherto, there have been far fewer attempts to develop a predictive numerical
89 model for the relevant physics of non-Newtonian droplets generation in a Newtonian
90 bulk phases. However, there is no unique constitutive model that can represent the
91 different characteristic behaviours of non-Newtonian fluids.

92 In microfluidics, the geometry of droplet interface is usually complex and it can
93 undergo large deformations or even topology changes such as fission and fusion in

94 microchannel. There are two approaches, namely interface tracking (Hou, Lowengrub,
95 & Shelley, 2001; Tryggvason et al., 2001) and interface capturing (Bonometti &
96 Magnaudet, 2007), to represent the flow problem of droplet interface evolution or
97 moving boundaries either explicitly or implicitly to the incompressible Navier-Stokes
98 equation discretised on a fixed grid. Interface tracking of the moving boundary in
99 multiphase system is an explicit representative that requires the computational
100 meshes to track the evolving interface for each time-step. In contrast, the interface
101 capturing approaches is an implicit representative that uses a phase function
102 discretised on the fixed grid to represent the interface (Bonometti & Magnaudet, 2007).
103 In present paper, conservative level-set method (LSM) is adopted as it is a simple and
104 robust scheme of interface capturing approaches for tracking moving interfaces and
105 shapes (Osher & Sethian, 1988). It permits numerical computations of such objects
106 involving curves and surfaces to be performed on a fixed Cartesian grid without having
107 to parameterize them (Olsson & Kreiss, 2005; Olsson, Kreiss, & Zahedi, 2007; Osher
108 & Sethian, 1988). In the LSM, the surface tension force is conventionally modelled as
109 a distributed body force though concentrated in a band around the interfaces. The
110 variation of surface tension force across the interface can be difficulties in the
111 application of others common interface capturing methods, including the volume-of-
112 fluid (Rider & Kothe, 1998) (VOF) and lattice-Boltzmann method (LBM) (Takada,
113 Misawa, Tomiyama, & Fujiwara, 2000). However, the LSM can resolve to the
114 challenges of mass conservation and the treatment of discontinuities across the
115 flexible interface (Olsson & Kreiss, 2005; Olsson et al., 2007).

116 The present paper demonstrates systematic sets of numerical simulations for the
117 microdroplet generation of a shear-thinning Na-CMC droplets in Newtonian flow at a
118 microfluidic T junction using a developed predictive computational model. The present
119 model is adopted with the integration of conservative level-set approach and non-
120 Newtonian constitutive law. Fundamental principles and application of microfluidic
121 systems were presented due to the selection and interpretation of the subsequent
122 numerical analysis. Numerical simulations of the Na-CMC microdroplets formation in
123 an olive oil-based continuous phase were carried out. The present study reveals the
124 interesting phenomena of shear-thinnings droplet formation during the systematic
125 variation in flow rates, interfacial tension, and surface wettability. As a result, the
126 rheological characteristics of Na-CMC solution are strongly depending on its

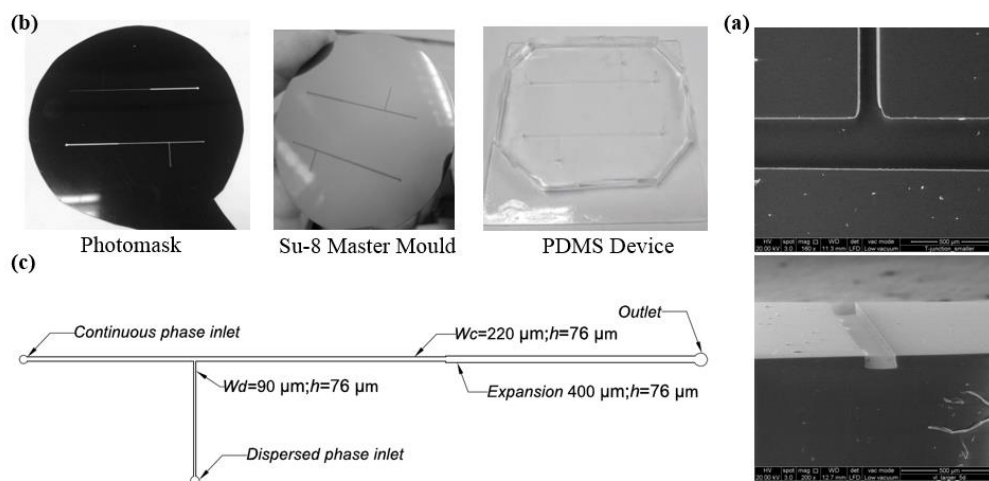
127 concentration. Thus, the impact of these rheological characteristics of Na-CMC can
 128 be of great interest to provide an insightful understanding to the relevant physics of
 129 non-Newtonian droplet formation process in microfluidic flow.

130

131 2. Experimental Methodology

132 2.1 Microfluidics Device Fabrication

133 A channel dimension of $220\ \mu\text{m}$ (w_c) \times $90\ \mu\text{m}$ (w_d) \times $76\ \mu\text{m}$ (h) was used in present
 134 validation studies. It was fabricated in-house by photolithography and soft lithography
 135 technique. Fig. 1 illustrates the dimensions of a T-junction employed in the numerical
 136 and experimental studies. Prior to the start of fabrication process, an out sourced
 137 positive photolithographic mask (clear lines with a black background) was used to
 138 transfer of the photo-lithographically pattern onto the negative mould. The
 139 photolithographic mask with the desired layout of microchannel structure was
 140 designed using standard computer assisted design (CAD) program. The
 141 polydimethylsiloxane (PDMS) mould was fabricated by moulding a mixture of PDMS
 142 liquid pre-polymer, a 10:1 mixture of Sylgard 184 silicone elastomer and curing agent
 143 (Dow Corning, USA), onto the SU-8 master mould with SU-8 2025 (MicroChem
 144 Corporation, Newton, MA) as the photoresist that ultimately becomes the pattern on
 145 the silicon wafer. The glass slide with a cured PDMS thin layer and the surface of the
 146 PDMS mould with the micropattern indent then brought into conformal contact before
 147 flow experiment was conducted.



148

149 **Fig. 1:** Illustration of (a) microfluidics T-junction composed of rectangular channels; (b)
 150 schematic diagram of microfluidics T-junction composed of rectangular channel; (c)

151 Scanning electron microscope (SEM) image of fabricated T-junction of PDMS
152 microchannel and cross section of PDMS microchannel.

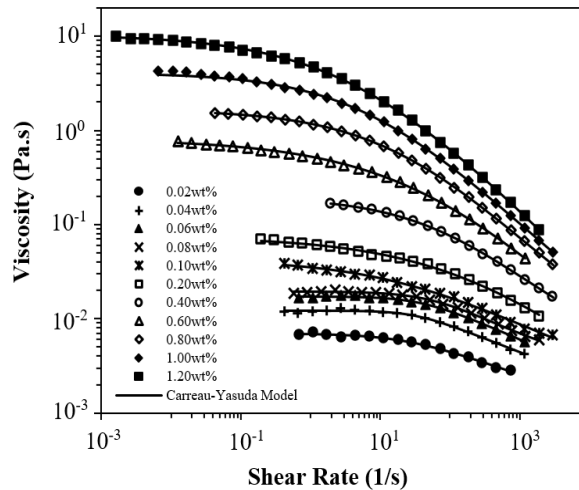
153

154 **2.2 Fluid Characterisation**

155 A calibrated BS/U-tube viscometer was used to perform the kinematic viscosity
156 measurement for the transparent Newtonian olive oil (Sigma Aldrich). The capillary
157 diameter of BS/U-tube viscometer with $0.50 \text{ mm} \pm 0.01 \text{ mm}$ was used. The
158 viscometers were mounted upright in a beaker (2000 mL) of water at controlled room
159 temperature ($20 \pm 2^\circ\text{C}$). Each sample solutions were allowed to attain the room
160 temperature for 10 minutes. The viscosity measurements for Newtonian solution were
161 conducted three times, and average values were taken for analysis. For shear-
162 thinnings Na-CMC ($[\text{C}_6\text{H}_7\text{O}_2(\text{OH})\text{CH}_2\text{COONa}]_n$, Sigma Aldrich) aqueous solution, the
163 rheological measurements were performed on controlled stress rheometer (MCR 302,
164 Anton Paar) equipped with a cone-and-plate geometry (cone plate with diameter of 50
165 mm; angle 0.04 radian) at controlled temperature of 20°C . The samples were carefully
166 loaded onto the measuring plate of the rheometer and left to idle for 10 minutes prior
167 to viscosity measurement. Fig. 2 illustrates the shear viscosity against shear rate plot
168 of Na-CMC solutions at various concentrations ranging from 0.02 wt% to 1.20 wt%
169 has been plotted over a log-log scale that covers nearly six orders of magnitude of
170 shear rate (Wong, Loizou, Lau, Graham, & Hewakandamby, 2017). In present work,
171 power-law model is not potentially selected to describe the behaviour of shear-
172 thinnings working fluid of Na-CMC aqueous solution as it poses limitations on its range
173 of applicability over a wide range of shear rate. In order to circumvent the drawback of
174 the power-law model, alternative approaches such as Carreau-Yasuda model utilize
175 viscosity functions that have finite values both at very low and high shear rate
176 (Chhabra & Richardson, 2008). Additionally, all the measurement data were well-fitted
177 to the well-known Carreau-Yasuda model (Chhabra & Richardson, 2008) for the shear-
178 thinnings behaviour of Na-CMC:

$$179 \eta(\dot{\gamma}) = \eta_\infty + (\eta_0 - \eta_\infty) [1 + (\lambda_{CY} \dot{\gamma})^a]^{\frac{n-1}{a}} \quad (1)$$

180 where η_0 is zero shear viscosity, η_∞ is infinite shear viscosity, λ_{CY} is the relaxation time,
181 $\dot{\gamma}$ is shear rate, n is power-law exponent and a is the fitting parameter for Carreau-
182 Yasuda model.



183

184 **Fig. 2:** Shear viscosity plotted against shear rate for a series of Na-CMC shear-
 185 thinning solutions with different concentrations (Wong et al., 2017).

186

187 **2.3 Emulsification Setup**

188 The continuous (olive oil) and dispersed phase liquids (Na-CMC aqueous) were
 189 dispensed separately into the reservoirs of microchannel; each fluid was driven
 190 through microchannel at the desired continuous (Q_c) and dispersed flow rates (Q_d)
 191 using syringe pumps (AL-1000, Florida and NE-1000, Netherlands), respectively. The
 192 processes before and after droplet formation in microfluidics device were recorded
 193 using a high speed camera (MIC Hotshot 1280 cc) connected to an epifluorescence
 194 microscope (Olympus IX51, Japan). The experimental setup with flow visualisation is
 195 illustrated in Fig. 3. After stabilizing the system for predetermined time intervals (20
 196 minutes), videos were recorded at 500 frames per second (fps) after each flow rates
 197 of either continuous or dispersed phase were adjusted. The average effective droplet
 198 diameter of 30 droplets under experimental condition was measured through an image
 199 processing routine using MATLAB. All the collected data will be validated prior to the
 200 parametric analysis.

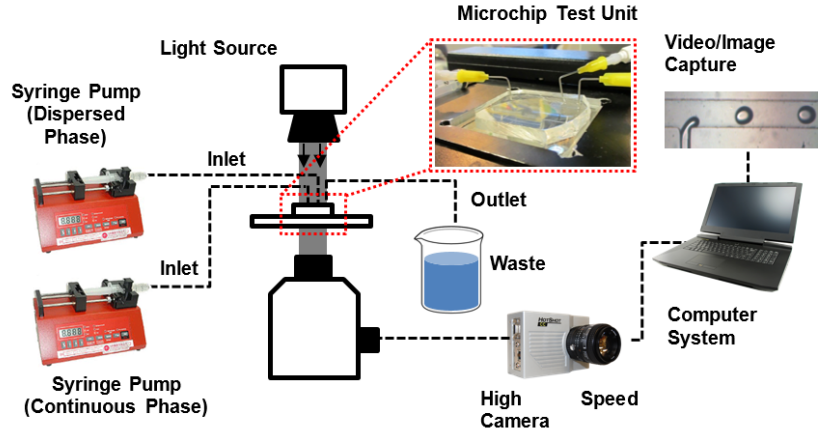


Fig. 3: Schematic diagram of experimental setup for flow visualization.

3. CFD Modelling and Simulation

3.1 Theory Model

A predictive numerical model was developed to track the fluid-fluid interfaces between two immiscible fluid phases of different density and viscosity. This applied the conservative LSM from CFD module using COMSOL Multiphysics. The mathematical model used in the computational fluidic dynamic simulation utilized a numerical time-stepping procedure to obtain the model behaviour over time. The governing equations for momentum and conservation laws of mass was considered, which was shown in the following forms with the assumption that the fluid is incompressible:

$$\rho \frac{\partial \mathbf{u}}{\partial t} + \rho (\mathbf{u} \cdot \nabla) \mathbf{u} = -\nabla p + \nabla \cdot \eta (\nabla \mathbf{u} + (\nabla \mathbf{u})^T) + F_{st} \quad (2)$$

$$\nabla \cdot \mathbf{u} = 0 \quad (3)$$

where ρ , η , and F_{st} denote the density, dynamic viscosity, and the surface tension force respectively, p denotes pressure while I is the identity matrix. Naturally, the Navier-Stokes equation (Equation (2)) is solved on the fixed grid to control the motion of multiphase system. The density and the viscosity of the two fluids at any point can be calculated using the two equations given below:

$$\rho = \rho_1 + (\rho_2 - \rho_1) \tilde{\phi} \quad (4)$$

$$\eta = \eta_1 + (\eta_2 - \eta_1) \tilde{\phi} \quad (5)$$

where ρ_1 and ρ_2 are the densities of continuous phase and dispersed phase, and η_1 and η_2 are the viscosities of continuous phase and dispersed phase. A smeared out approach is used where the discretisation of the Heaviside function ($H_{sm}(\phi)$) can be

226 useful as it is better suited to numerical computations (Deshpande & Zimmerman,
227 2006):

$$228 \quad \tilde{\phi} = H_{sm}(\phi) = \begin{cases} 0, & \text{if } \phi < -\varepsilon \\ \frac{1}{2} + \frac{\phi}{2\varepsilon} + \frac{1}{2\pi} \sin\left(\frac{\pi\phi}{\varepsilon}\right), & \text{if } -\varepsilon \leq \phi \leq \varepsilon \\ 1, & \text{if } \phi > \varepsilon \end{cases} \quad (6)$$

229

230 where ε denotes the interface thickness. The F_{st} term acting on the interface between
231 two fluid phases is determined by following equation:

$$232 \quad F_{st} = \sigma k \mathbf{n}_\Gamma \delta_{sm} \quad (7)$$

233 where σ denotes surface tension, k denotes local interfacial curvature, \mathbf{n}_Γ is the unit
234 normal vector to the interface pointing into the droplet, and the δ_{sm} denotes the
235 smeared out Dirac delta function (δ_{sm}) concentrated at the interface between two
236 fluids. These above parameters can be calculated by Equation 8, 9, and 10,
237 respectively:

$$238 \quad k = -\nabla \cdot \mathbf{n}_\Gamma \quad (8)$$

$$239 \quad \mathbf{n}_\Gamma = \frac{\nabla \phi}{|\nabla \phi|} \quad (9)$$

$$240 \quad \delta_{sm}(\phi) = \begin{cases} 0, & \text{if } \phi < -\varepsilon \\ \frac{1}{2\varepsilon} + \frac{1}{2\varepsilon} \cos\left(\frac{\pi\phi}{\varepsilon}\right), & \text{if } -\varepsilon \leq \phi \leq \varepsilon \\ 0, & \text{if } \phi > \varepsilon \end{cases} \quad (10)$$

241 To retain the level-set function (ϕ), a re-initialization procedure is required for the finite
242 element approximation of the level-set equation. A re-initialized and conservative
243 level-set method is used to describe and convect the fluid interface. The following
244 equation describes the convection of re-initialized level-set function:

$$245 \quad \frac{\partial \phi}{\partial t} + \mathbf{u} \cdot \nabla \phi = \gamma \nabla \cdot \left[\varepsilon \nabla \phi - \phi(1-\phi) \frac{\nabla \phi}{|\nabla \phi|} \right] \quad (11)$$

246 where γ and ε are numerical stabilization parameters, where the former denotes re-
247 initialization parameter and latter parameter determines the thickness of the interface.
248 Equation (11) is coupled to the governing equations (Equation (2) and (3)) in present
249 numerical model. The γ approximates the maximum speed occurring in the
250 computational domain. The ε assumed as the maximum mesh size in subdomains in
251 the neighbourhood of the interface. After the grid convergence analysis, the

252 parameters γ and ε with the value of 0.065 m/s and 5.8×10^{-6} m were calculated based
 253 on the maximum flow velocity in microchannel and optimum mesh size, respectively.

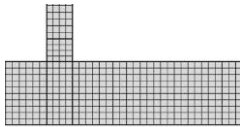
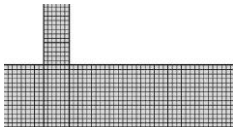
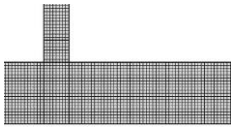
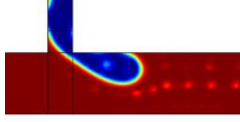
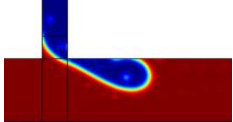
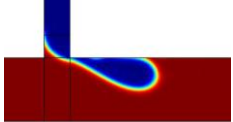
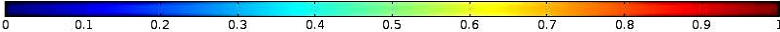
254

255 3.2 Domain Discretisation and Grid Convergence Analysis

256 A T-shaped geometry with prescribed dimension of $220 \mu\text{m} \times 90 \mu\text{m}$ was created and
 257 meshed with quadrilaterals elements. An entrance thickness (h) of $73.5 \mu\text{m}$ was
 258 prescribed in numerical system define the depth of the microchannel. The typical finite
 259 element mesh for structured mesh of two-dimension (2D) mapped mesh for a 2D
 260 model was selected. Mesh refinement analysis were performed to quantify the
 261 dependency of simulation results on the grid size and achieve an optimal grid
 262 resolution. Meshes of varying degrees of resolution were set up for the T-junction
 263 domain with the same grid size of near-wall region. Table 1 illustrates three examples
 264 of mesh geometry with prescribed dimensions in COMSOL Multiphysics. Mesh can be
 265 arranged as to be clustered near the wall for optimum grid resolution in order to resolve
 266 the boundary layer flow in future work.

267

268 **Table 1:** Comparison of a T-shaped geometry with coarser and finer mesh size.

No. of Mesh Elements	976 (Coarse)	2072	4024 (Finer)
2D Structured Mapped			
Mesh			
Two-phase Flow at $t=0.05\text{s}$ and $Q=0.05$ ($Q_c:2.0\text{ml/hr}$; $Q_d:0.1$ ml/hr)			
	 Surface Volume Fraction		

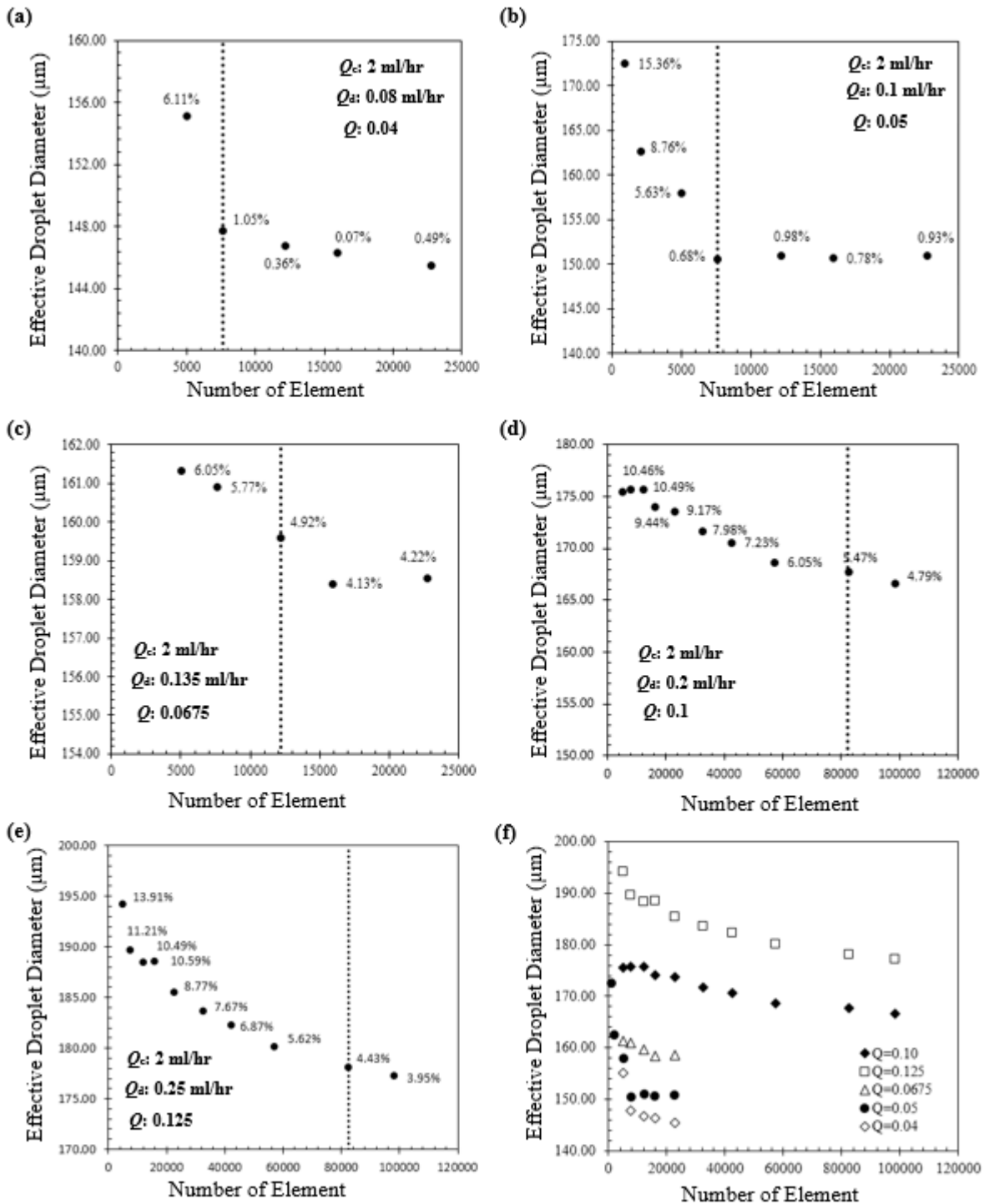
269

270 The present model is set up for transient analysis which provides the time domain
 271 response of a system subjected to time-dependent loads. The effect of mesh size was
 272 examined by increasing the number of mesh elements from initial number of elements
 273 of 976 (coarsest) to 98184 (finest). Finer grid size are generated by simultaneously
 274 increasing the number of nodes in all direction to obtain as close to a uniform
 275 refinement. The number of elements is increased by a mean factor of $\sqrt{2}$ for each
 276 refinement settings. Thus, the total number of nodes for each refinement is

277 approximately doubled over the previous grid size. Preliminary test of grid
 278 convergence analysis was solely carried out at flow rate ratio, Q of 0.05, which is a
 279 quotient of a flow rate of the flow for dispersed phase and continuous phase. An
 280 acceptable relative error and error percentage of 0.15% and $\leq 1\%$ between the last
 281 two finer grids (12166 and 15963) was obtained, respectively. Fig. 4(b) illustrates the
 282 grid convergence analysis at Q of 0.05. An optimal simulations results was achieved
 283 at 7644 number of elements. The relative error of measurements shows the error
 284 deviation in relation to the effective droplet diameter between each mesh resolutions.
 285 While the error percentage of measurements shows the error deviation in relation to
 286 the effective droplet diameter between numerical and experimental data. In the
 287 present work, all the parametric studies used, as key output, the effective droplet
 288 diameter. Therefore, an integration operator was added to find the area corresponding
 289 to the dispersed phase, where $\tilde{\phi} \geq 0.5$, in order to calculate the effective droplet
 290 diameter by the following equation:

$$291 \quad d_{eff} = 2 \cdot \sqrt{\frac{1}{\pi} \int_{\Omega} (\tilde{\phi} > 0.5) d\Omega} \quad (12)$$

292 This is the diameter of a spherical droplet that has equivalent volume of the formed
 293 droplet. The extensive studies of grid convergence analysis was also performed on
 294 different flow rate ratio. Fig. 4 illustrates the mesh dependence profile with error
 295 percentage of droplet size measurement at different flow rate ratio Q . For a constant
 296 Q_c at 2.00 ml/hr, the effective droplet diameter was measured with the variation in Q_d
 297 (0.08 ml/hr to 0.125 ml/hr) for various number of elements. As seen in Fig. 4, the results
 298 of convergence are found to achieve more rapidly and effectively in cases at lower
 299 flow rate ratio ($Q \leq 0.0675$). Higher flow rate ratios are limited to a certain range in
 300 numerical model due to difficulties of numerical dissipation in the advection step of
 301 fluid simulation. Moreover, further refinement is required to sufficiently resolve the
 302 higher velocity profiles. Thus, the subsequent parametric studies were mainly based
 303 on Q of 0.05 at optimal mesh size. Particularly, the numerical simulations were
 304 performed at a time-step size of 2.57×10^{-5} seconds calculated using the Courant-
 305 Friedrichs-Lewy (CFL) conditions. It shows a relation between the computational cell
 306 size, the transient time-step size, and the fluid velocity within the cell. A Courant
 307 number of 0.25 is selected in the present study considering as robust value to maintain
 308 the stability of calculations.



309

310 **Fig. 4:** Grid convergence analysis for different flow-rate ratio profile: (a) $Q=0.04$; (b)
 311 $Q=0.05$; (c) $Q=0.0675$; (d) $Q=0.1$; (e) $Q=0.125$; (f) combination of mesh refinement
 312 profile.

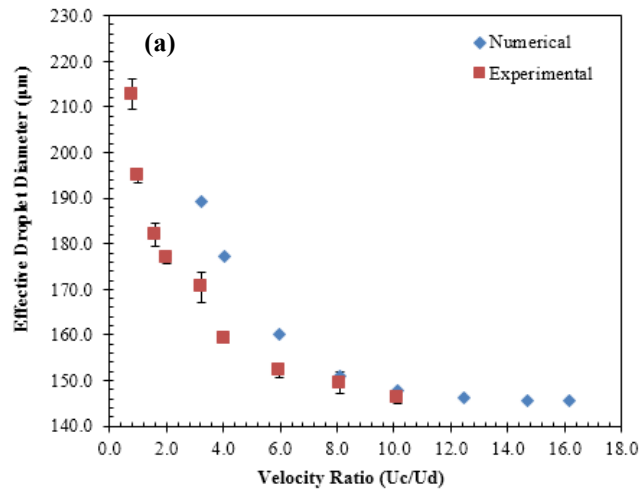
313

314

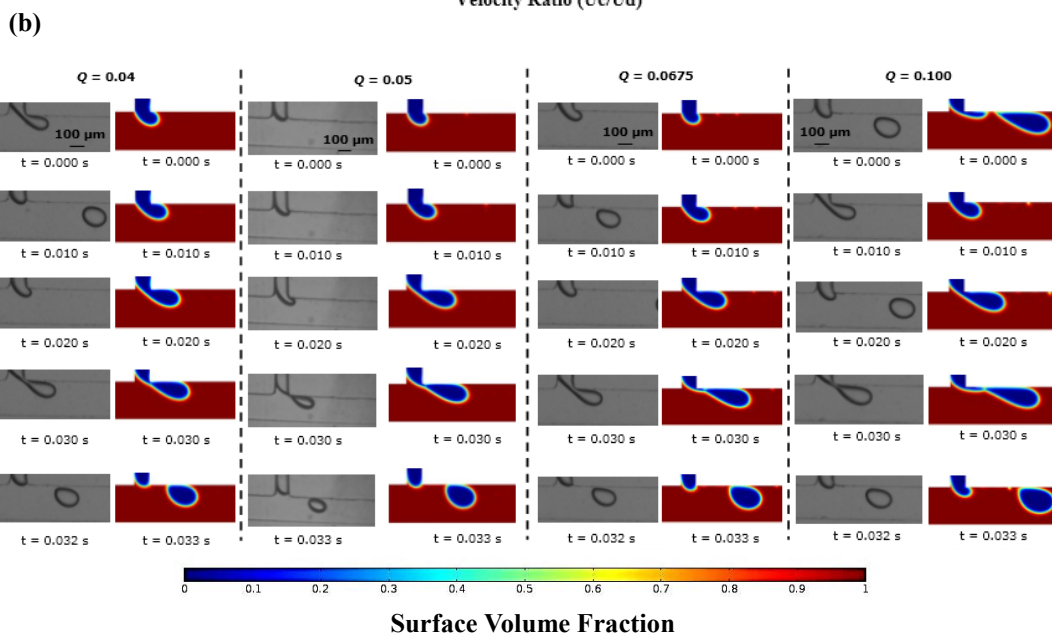
315 3.3 Numerical Model Validation with Experimental Justification

316 Mesh convergence analysis was studied to quantify the dependency of simulation
 317 results on mesh size and achieve an optimal grid resolution of 7644. A preliminary

318 validation of numerical simulations of the formation of deionized water droplets in olive
 319 in a T-junction microchannel was carried out and gave qualitative agreement with
 320 laboratory experimental data to predict with reasonable accuracy in the range of
 321 velocity applied. The results of convergence is found to be achieved more rapidly at
 322 lower flow rate ratio. Fig. 5 illustrates the variation in effective droplet diameter
 323 between the experimental and numerical studies.



324



325

326 **Fig. 5:** Comparison of (a) effective droplet diameter between numerical and
 327 experimental result in the range of velocity ratio applied. Error bars shown indicates
 328 the standard deviation in droplet size measurement of 30 droplets under fixed
 329 experimental condition. Dashed box shown denotes the (b) droplet breakup
 330 phenomena in the range between Q of 0.04 and 0.1.

331

332

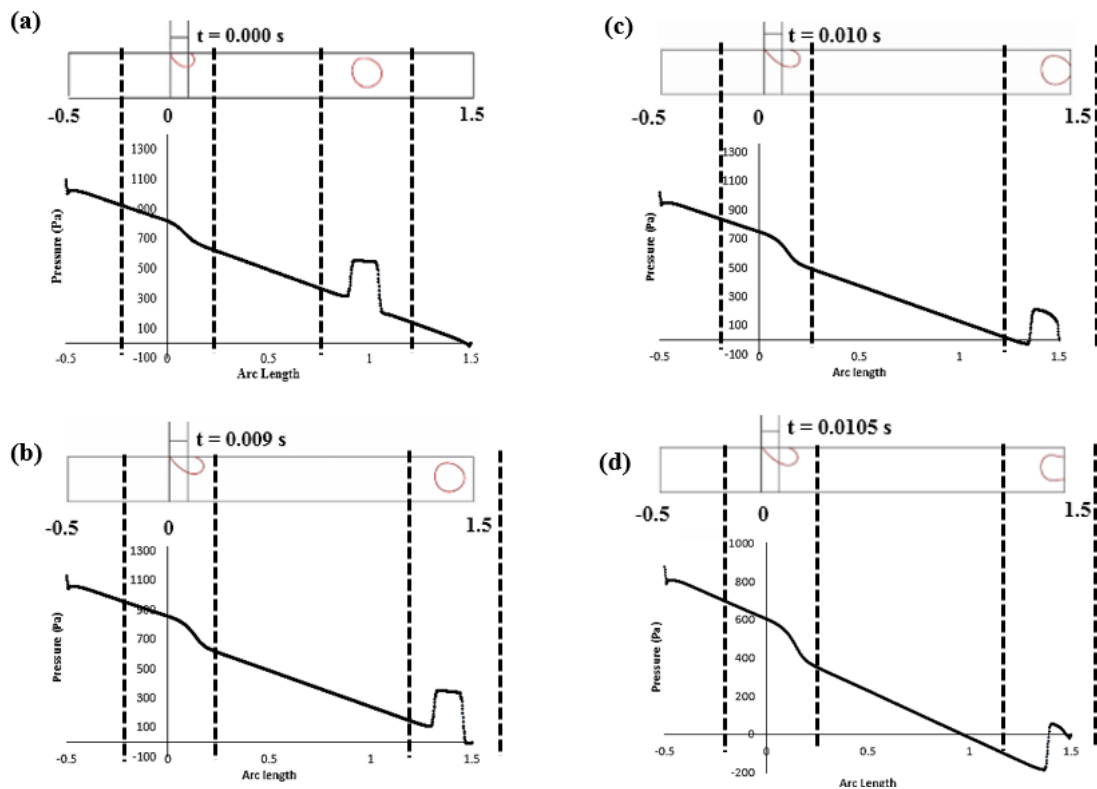
333 The data was recorded at 5×10^{-3} seconds intervals to capture the growth and
 334 detachment phenomenon of the fluid-fluid interfaces. A contact angle of 180° that

335 represents the complete repulsion of Na-CMC droplets by the PDMS with hydrophobic
 336 channel wall surface was applied in the computation. As can be seen in Fig. 5, the
 337 numerical simulation of detachment process was shown in similar manner with the
 338 experimental data at $Q < 0.0675$. Nevertheless, such an agreement was physically
 339 unreasonable at higher Q as jet breakup phenomena is found to be more significant
 340 for numerical simulation over time. This might be due to the numerical dissipation
 341 increases the viscosity of working fluid and causes it appear more viscous than
 342 intended at higher Q . Thus, the Q of 0.05, as equivalent to the velocity ratio (u_c/u_d) of
 343 8, was adopted in present parametric studies subsequently.

344

345 3.4 Simulated Laplace Pressure of Droplet Interface Profile

346 First, the static pressure is decreasing linearly along the cross-sectional 2D plane of
 347 the microchannel. Fig. 6 illustrates the pressure drop distribution along the channel a
 348 droplet containing with 0.02 wt% Na-CMC solution.



349

350 **Fig. 6:** The pressure distribution of a generated 0.20wt% Na-CMC droplet interface
 351 along the T-junction microchannel at Q of 0.05.

352

353 In the presence of curved interfaces, the curvature induce a pressure jump, which is
 354 known as Laplace pressure. The Laplace pressure jumps was determined in the path

355 across the droplet body while crossing the front and rear interfaces. As the dimension
356 of the interest gets smaller, surfaces tension becomes dominant over gravitational
357 forces and others physical forces such as viscous and inertial forces. The surface
358 tension becomes an important surface energy parameter that controls the stability of
359 interfaces between the two phases when the droplets are forming. Due to the
360 existence of surface tension effect in a case of a liquid droplet, the Laplace law implies
361 a greater pressure inside the droplet than a continuous phase. As the radius of the
362 droplet become smaller, the pressure becomes larger on the concave side of liquid
363 interface. A Young-Laplace equation is usually used to determine the pressure
364 difference across a fluid interface as a function of curvature. Moreover, the magnitude
365 of this pressure differential can be expressed in term of surface tension:

$$366 \quad \Delta P_L = \sigma \left(\frac{1}{R_1} + \frac{1}{R_2} \right) \quad (13)$$

367 where σ is the surface tension of the respective liquid interface and R_1 and R_2 are the
368 two principal curvature radii of the interface. Additionally, the effect of viscous
369 dissipation inside the droplets may also prominently affects the pressure drop
370 distribution when the viscous effect is considerably increased.

371

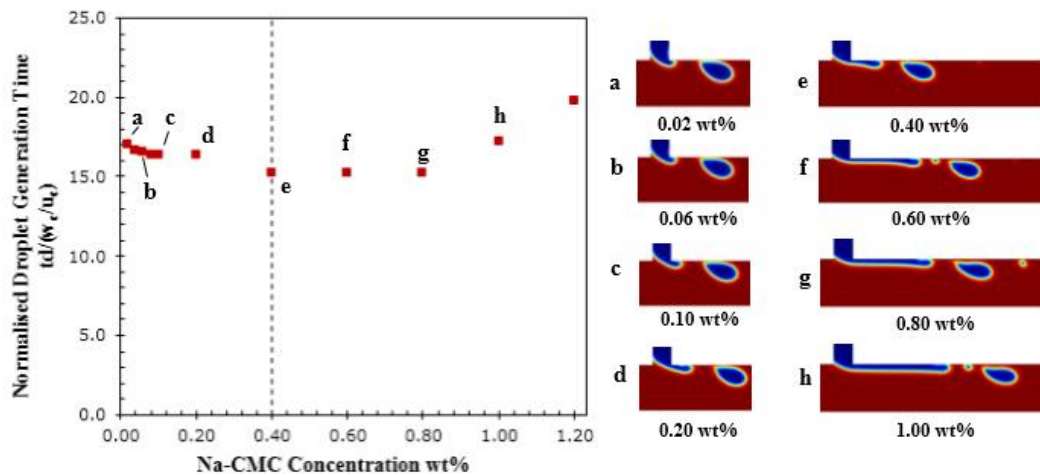
372 **4. Results and Discussion**

373 **4.1 Effect of Na-CMC Viscosity on Droplet Breakup Time and Production Rate**

374 The present investigation was designed to determine the Na-CMC viscosity effect on
375 the droplet breakup time and production rate. The viscosity of polymer solution is a
376 function of concentration and the molecular weight of dissolved polymer. While the
377 concentration of Na-CMC solution is increased in a series of simulations from 0.02
378 wt% to 1.20 wt% at a constant Q of 0.05, the evolution of droplet breakup time can be
379 discerned in two distinct non-monotonic behaviour. Fig. 7(a) illustrates the Na-CMC
380 concentration effect on the normalized droplet breakup time whereas the normalized
381 production rate is shown in Fig. 7(b). The variation of viscosity of a shear thinning drop
382 occurs during the pinch off process. Initially, the breakup time decreases as Na-CMC
383 concentration increases from 0.02 wt% to 0.40 wt%. The shear-thinning effect of Na-
384 CMC solution increases with the concentration. The greater shear-thinning effect may
385 exhibit a decrease in polymer viscosity upon the application of shear near the channel
386 wall due to the inertial force. At concentrations well above 0.40 wt%, the Na-CMC

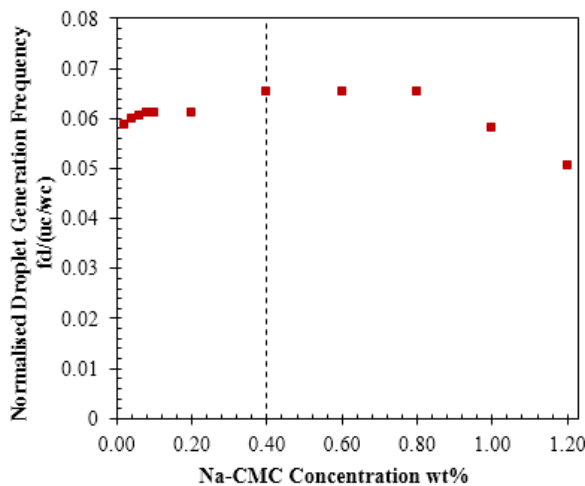
387 droplet breakup time increases may to the viscous force becomes significantly
 388 prevailing over the inertial force induced by the continuous phase on the forming
 389 interface. In general, the largest shear rate occurs at the corner edge of the T-junction
 390 and thus the shear-induced destabilization of the dispersed thread causes the breakup
 391 of thread leading to the formation of droplets. As can be seen in Fig. 8, the distribution
 392 of non-Newtonian wall shear-rate decreases as compared to the Newtonian wall shear
 393 rate profile. While in the lower wall shear rate range, the Na-CMC solutions exhibited
 394 a significant increase in viscosity. This means the low shear rate viscosity occurs at
 395 the high concentration of Na-CMC content. Consequently, the droplets pinch-off in
 396 larger viscosity fluids for which the inertial effects are unamplified.

397 (a)



398

399 (b)



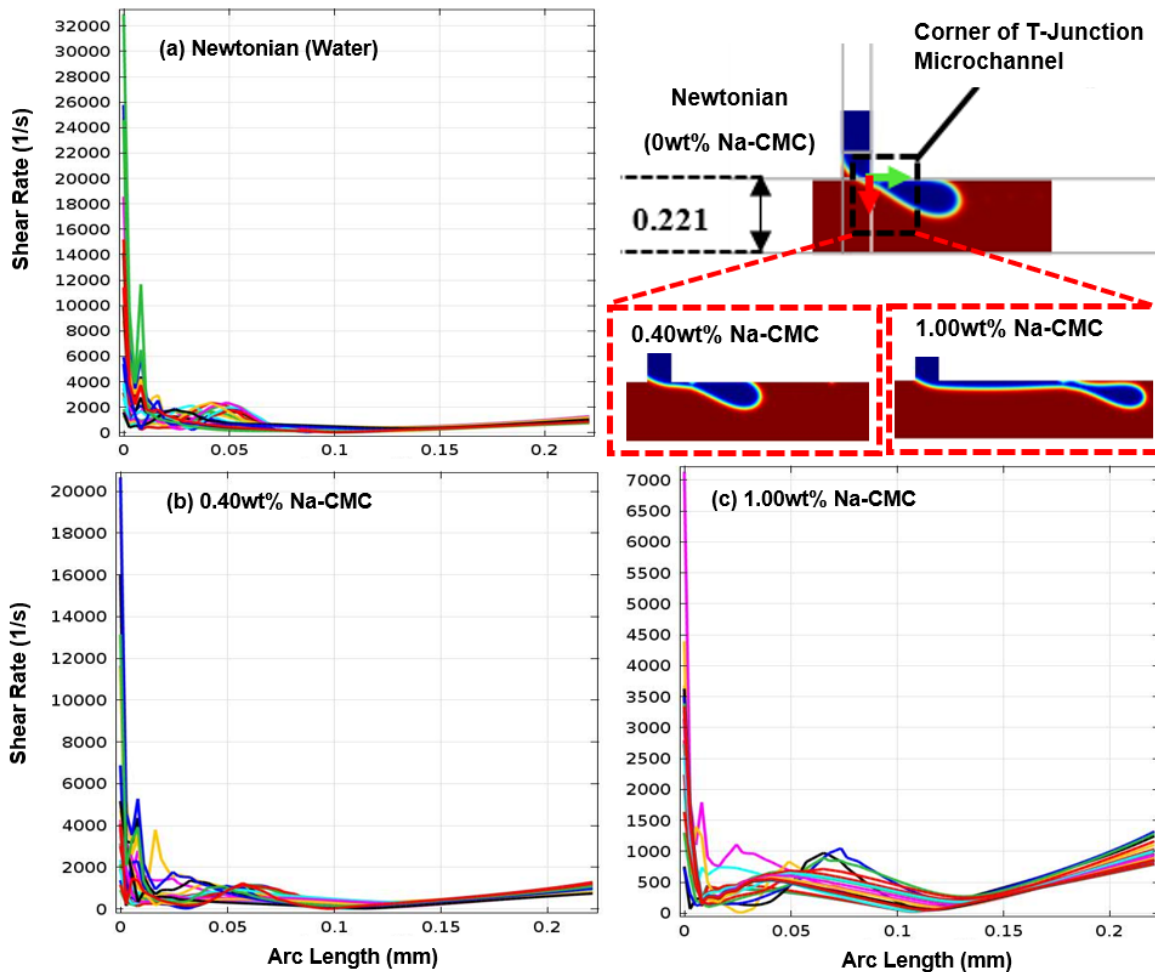
400

401 **Fig. 7:** Effect of Na-CMC concentration on (a) droplet breakup time (b) droplet
 402 production rate (for system: $Q_d/Q_c=0.05$).

403

404 At dilute Na-CMC concentrations below 0.40 wt%, the viscosity effect is not
 405 considerable as the direct intermolecular interactions are negligible. As the Na-CMC

406 concentration increases, the shear-thinning effect becomes more significant and
407 causes rapid pinch-off due to the high shear stress exerted by the continuous phase
408 near to the wall. The viscosity of the shear thinning drop is reduced when the drop
409 begins to neck response to the increased shear rate in that region. As the neck
410 continues to thin, the region of lower viscosity grows to encompass almost the entire
411 drop occurring within the neck and just outside it where the outflows from the neck
412 occur (Malcolm R. Davidson & Cooper-White, 2006; M. R. Davidson, Cooper-White,
413 & Tirtaatmadja, 2004). Nevertheless, extending breakup occurs and lower production
414 rate was found for the Na-CMC solution concentration above 0.40 wt%. This is mainly
415 caused by the development of entanglement coupling between the polymer chains,
416 which begins manipulating the fluid characteristics of Na-CMC solution. The
417 elongation of the necking into a thin filament connect between the primary droplet and
418 the upper dispersed phase thread, suggest that an increase in polymer concentration
419 which plays an important role in resisting drop pinch-off with the formation of thinning
420 filament. Thus, the viscous fluid thread is then stretched by the mainstream flow to the
421 downstream region and the breakup event is delayed substantially.



422

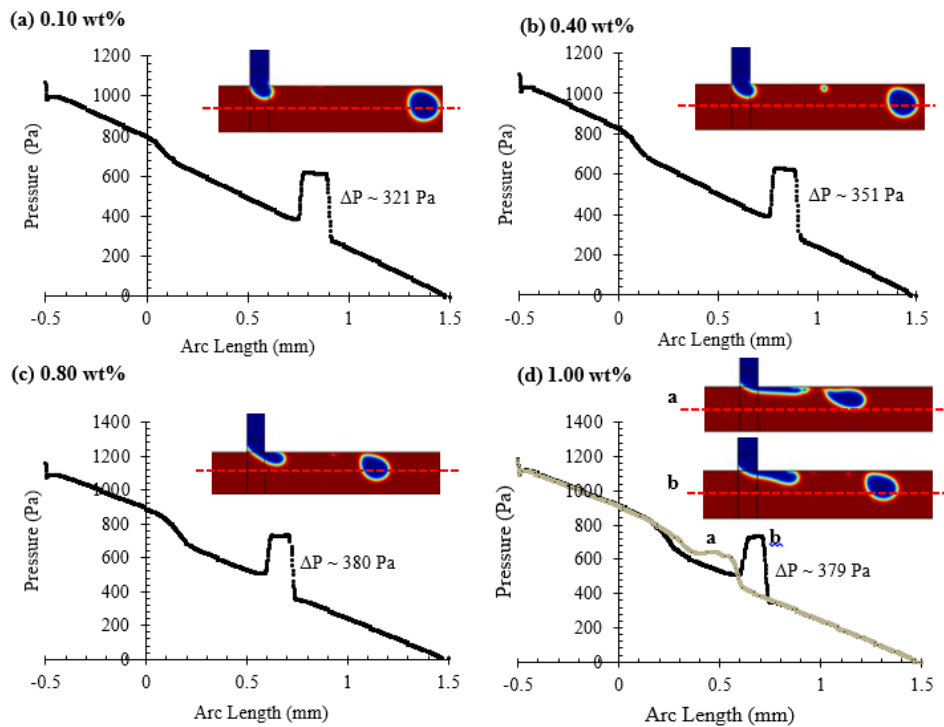
423 **Fig. 8:** Shear rate profile of fluid flow at the edge of T-junction microchannel along the
 424 arc length of continuous phase for (a) Newtonian system; (b) 0.40wt% Na-CMC non-
 425 Newtonian system; and (c) 1.0 wt% Na-CMC non-Newtonian system (for system:
 426 $Q_d/Q_c=0.05$).

427

428 Fig. 9 illustrates the Laplace pressure profile of a Na-CMC droplet interface curvature
 429 for different polymer concentrations at the middle plane of the microchannel. At dilute
 430 Na-CMC concentration below 0.40 wt%, droplets are self-propelled some distances
 431 from the wall mainly subjected to the gradient of the surface energy and higher velocity
 432 flow stream of the main channel after the sharp breakup occurs at the corner of T-
 433 junction. For the larger concentration of Na-CMC ($C > 0.40$ wt%) dispersed fluid, the
 434 presence of instabilities promotes the breakup of jets. After the formation of the primary
 435 breakup droplets, the generated droplet moves near the wall of microchannel as it is
 436 initially exposed to the flow projected from the side branch at the moment of breakup.
 437 After a certain distance, it will flow near the center of the bulk phase. The droplet with
 438 a radius in an emulsion will exert greater pressure on the inner concave interface than
 439 on the convex side. When the droplet deformation occurs, the Laplace pressure of the

440 deformed droplet is a function of the radius along the droplet surface (see section 3.4).
441 Thus, as the dispersed thread is elongated, a smaller droplet will be formed causing
442 smaller radius of curvature that result in a larger inward force and expected to
443 experience a greater pressure (see Fig. 9).

444



445

446 **Fig. 9:** A qualitative plot of the Laplace pressure profile of a generated Na-CMC droplet
447 interface curvature at concentration of 0.10 wt%, 0.40 wt%, 0.80 wt%, and 1.00 wt%
448 along the middle plane of microchannel (for system: $Q_d/Q_c=0.05$).

449

450 4.2 Effect of Surface Wettability on Droplet Breakup Time and Production Rate

451 The effect of shear-thinning nature on droplet breakup process has not been
452 extensively studied in the preceding analysis. In a T-shaped microchannel, the
453 continuous and dispersed phase were dispensed at the prescribed flow rates through
454 the microchannel with a hydrophobic wall surface ($\theta > 90^\circ$). Additionally, the
455 continuous phase needs to wet the surface of the channel walls preferentially in order
456 to repel the dispersed phase droplets away from the wall. The surface wettability of
457 microchannel are of utmost importance for the stability of the droplets formation
458 process in a microfluidic device. The effect of surface wettability on the total droplet
459 formation time, which is the transition between a growing and a detached droplet, was
460 discussed. Fig. 10 illustrates surface wettability effect on the normalized droplet
461 formation rate. Results revealed that the droplet detachment occurs more rapidly at

462 shorter times as the θ increases. The inertial force, shear force and surface wettability
463 are competing effects influencing the dynamics of the droplet breakup process. The
464 wettability driving the fluid toward the surface and the contact area between the
465 droplets and solid surface increases for the smaller θ . The smaller θ tends to reduce
466 the droplet deformation and delay the breakup process. As θ increases, the thread is
467 no longer flowing close to the wall as its adhesion strength to the wall reduces, causing
468 less resistance to flow. Therefore, the inertial force driving the flow of thread is
469 prevailing. The time for the formation of droplet is also essentially dependent of the
470 strength of shear force acting on the interface, because it dominates over the adhesion
471 force for larger θ . Bashir *et al.* (2011) reported that the degree of confinement promotes
472 the breakup for the larger θ ; whereas the degree of confinement suppresses the
473 breakup for smaller θ .

474

475

476

477

478

479

480

481

482

483

484

485

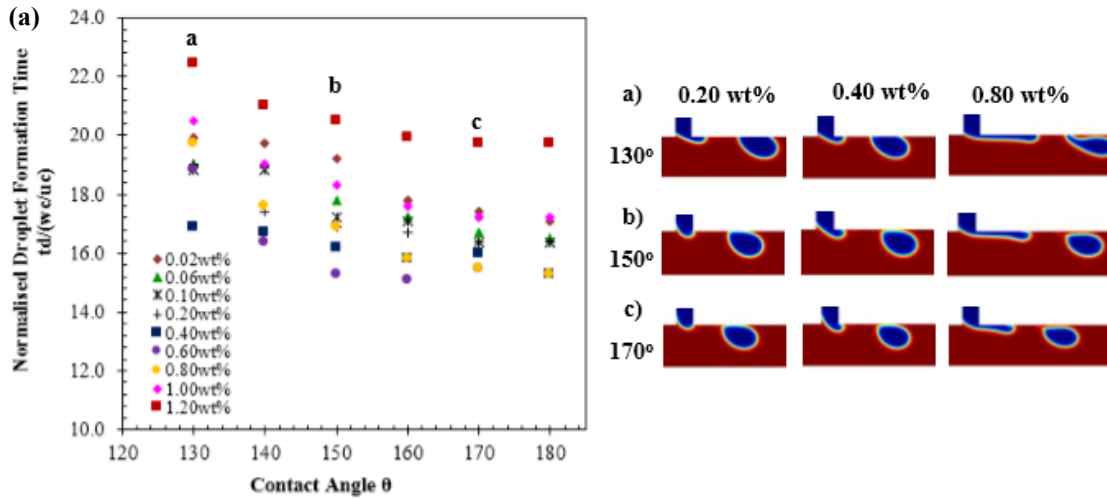
486

487

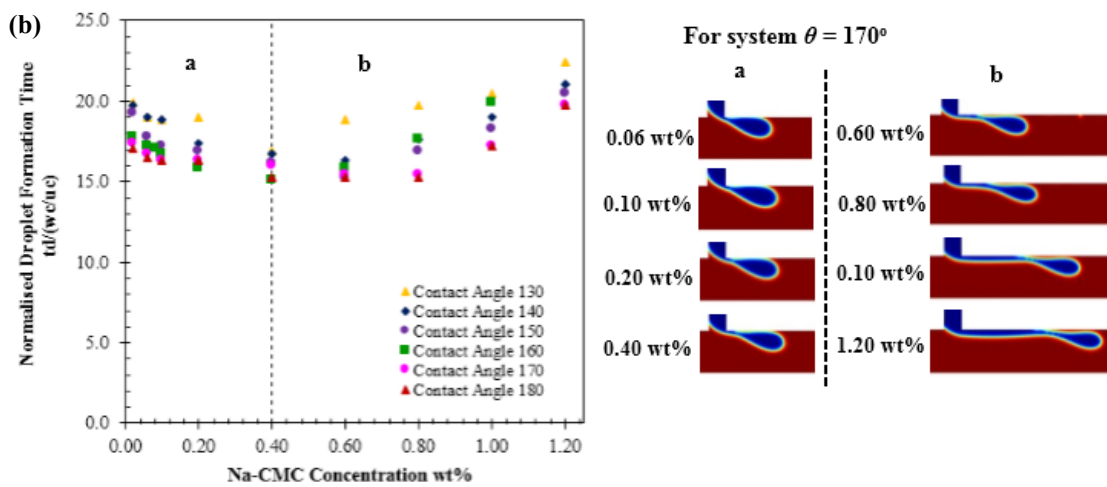
488

489

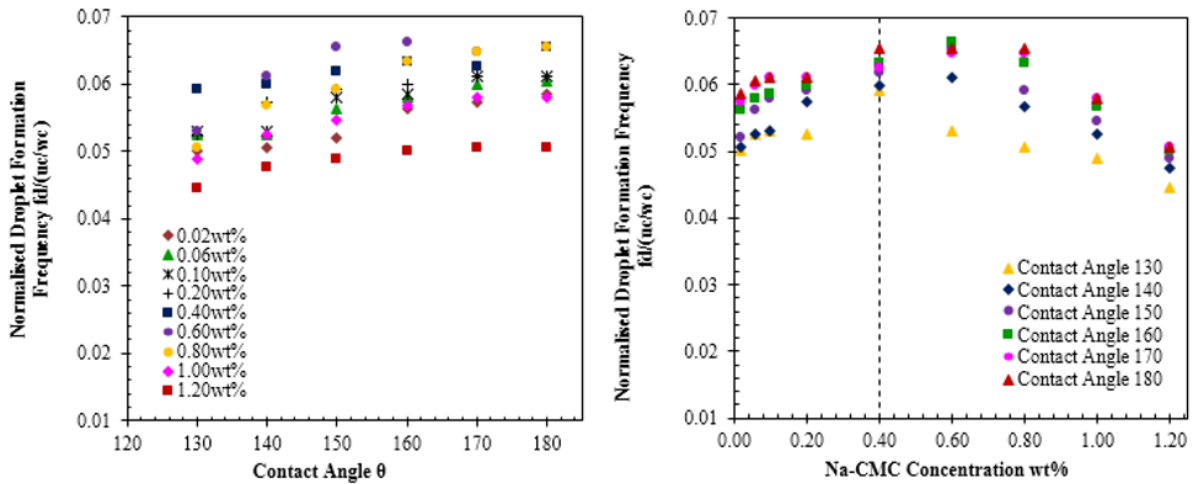
490



491



492



493

494 **Fig. 10:** (a) Effect of contact angle on the normalized droplet formation time of Na-
 495 CMC solutions. (b) Variation in normalized droplet formation rate of shear-thinning
 496 droplets for a. dilute ($C < 0.40$ wt%) and b. semi-dilute ($C > 0.40$ wt%) Na-CMC
 497 concentrations regime at fixed θ (for system: $Q_d/Q_c=0.05$).

498

499 For a fixed value of θ , the result reveals that the droplet formation time decreases as
500 the concentration of the Na-CMC increases from 0.02 wt% to 0.40 wt% (see Figure
501 10). Interestingly, a similar phenomenon does not happen for the larger concentration
502 ($C > 0.40$ wt%). This is due to the fact that the concentration of the polymer solutions
503 beyond the critical overlap concentration exert a significant influence on retarding the
504 droplet breakup time. As previously mentioned, the direct intermolecular interactions
505 can be neglected for low concentrations. Thus, the rapid pinch-off of shear-thinning
506 droplets occurring was due to the high shear stress in these low concentrations
507 regimes. When the Na-CMC concentration is increasing, the rheological behaviour of
508 Na-CMC solution may be governed by the development of entanglement coupling
509 between the chains and contribute significantly to the increasing of viscosity and the
510 formation of thinning filament.

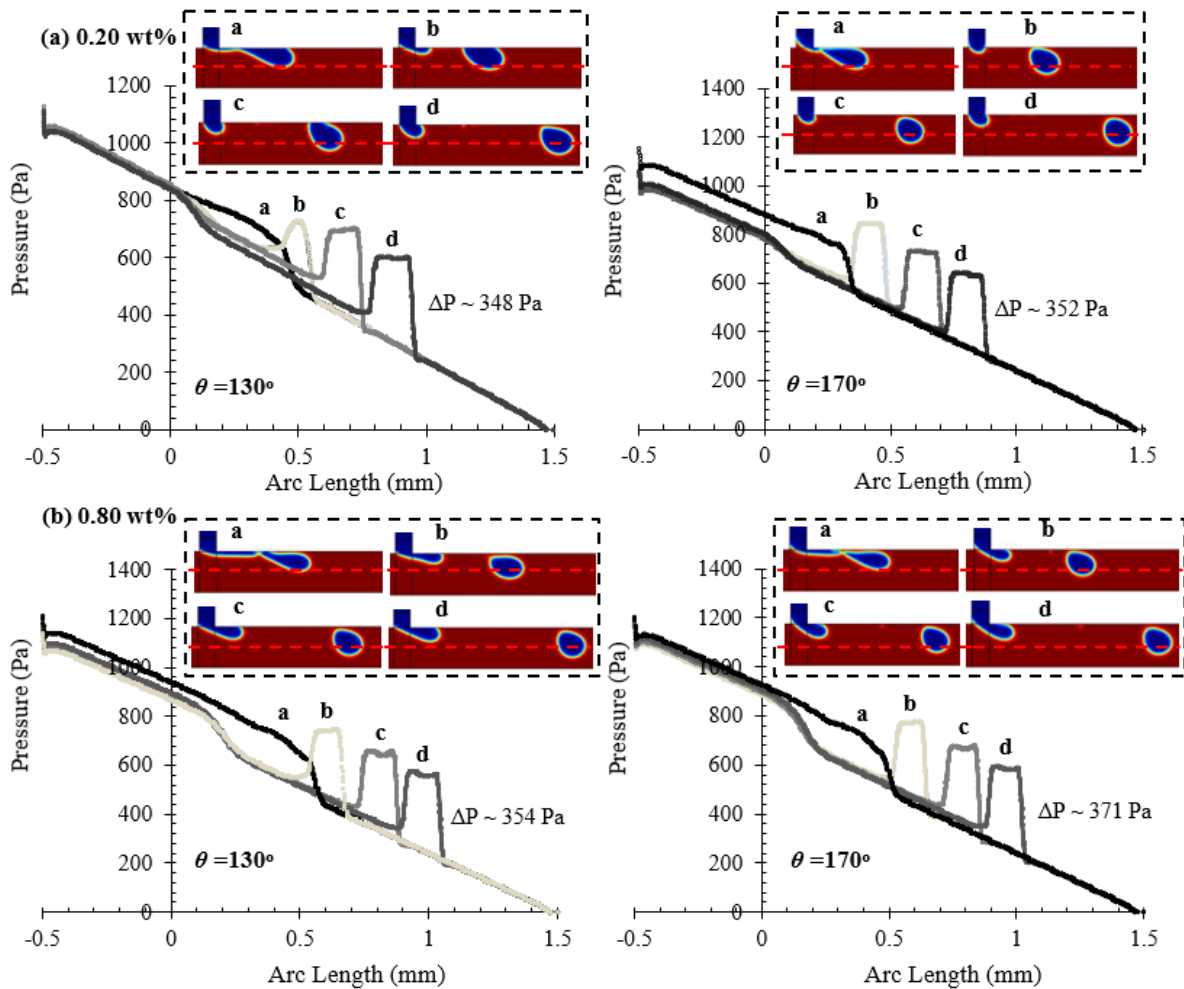
511

512 Hong and Cooper-White (2009) studied the effect of non-Newtonian Carbopol
513 dispersions on the droplet detachment behaviour in the bulk phase of silicone oil. The
514 Carbopol droplet pinch-off time increases with increasing the viscosity of dispersions³⁷.
515 Besides, Arratia *et al.*(2009) also reported that the time for polymer polyacrylamide
516 (PAA) droplet breakup was retarded as the polymer molecular weight is increased at
517 fixed Q (Hong & Cooper-White, 2009). Husny and Cooper-White (2006) also claimed
518 that pinch-off occurred rapidly without any significant filament formation during necking
519 for Newtonian droplet formation; but, this rapid necking event was retarded with the
520 formation of a thinning filament for polyethylene oxide (PEO) solutions (Husny &
521 Cooper-White, 2006). As can be seen in Fig. 10, a similar observation was found for
522 the higher Na-CMC concentration as the formation of a thin and stable filament
523 between the droplet and thread is more apparent when $C > 0.40$ wt%. The dynamics
524 of the thinning filament are governed by the shear stress and viscous pressure, by
525 which the filament is elongated drastically and resists the droplet pinch-off. Thus, the
526 delayed pinch-off may be due to the retardation effect of the fluid elasticity, which it
527 can be increased by increasing the polymer concentration. However, the entire
528 phenomena was observed from our predictive model with no elastic stress applied in
529 our present study. Hence, that shear-thinning alone is also sufficient to induce a
530 filament and that elasticity is not necessary.

531

532 In contrast, results revealed that the production rate of the Na-CMC droplet increases
533 with enhanced surface wettability. The droplet generation frequency increases with
534 dispersed phase concentration over the range of 0.02 wt% to 0.40 wt% when the
535 contact angle was held constant at each wetting condition. However, the rate of droplet
536 production begins to decrease with increasing the concentration of Na-CMC dispersed
537 phase concentration larger than 0.40 wt%, as noted in the previous section.

538 A comparison of pressure profiles of Na-CMC droplet at different contributions were
539 illustrated in Fig. 11. At low and dilute concentrations of the Na-CMC polymer, the
540 pressure drop of a stabilized curved surface of Na-CMC droplet is increasing along
541 the bulk phase with increasing the wetting conditions. The weak adhesion and strong
542 cohesion of the liquid in the bulk phase was found for the larger contact angles. The
543 unfavourability of channel surface to the dispersed thread plays and leads a major role
544 in the transport of droplet and lead to a larger shear force to be exerted on the drop
545 surface. Rapid deformation of the droplet occurs due to the adequate shearing force
546 induced by the continuous phase. Thus, the droplet mass was shown to decrease
547 when the initial contact angle is larger and leads to a larger pressure drop. The higher
548 concentration of Na-CMC dispersed phase contributes the same phenomenon. For
549 the Na-CMC concentration above 0.40 wt%, lower contact angles promote and
550 dampen greater spreading and dampens the breakup process. The spreading of the
551 elongated thread is eventually broken up into smaller droplets when the surface
552 energy is overcome. Neglecting the impact of fluid property on surface wettability, the
553 much larger concentration of fluid samples withdrawn from the dispersed thread can
554 create much greater pressure drop at the same contact angle.



555

556 **Fig. 11:** A qualitative plot of the Laplace pressure profile of a generated Na-CMC
 557 droplet interface curvature at concentration of 0.20 wt% and 0.80 wt%, along the
 558 middle plane of microchannel at $\theta = 130^\circ$ and 170° (for system: $Q_d/Q_c=0.05$).
 559

560

561

4.3 Effect of Interfacial Tensions on Droplet Breakup Time and Production

562

Rate

563

564

565

566

567

568

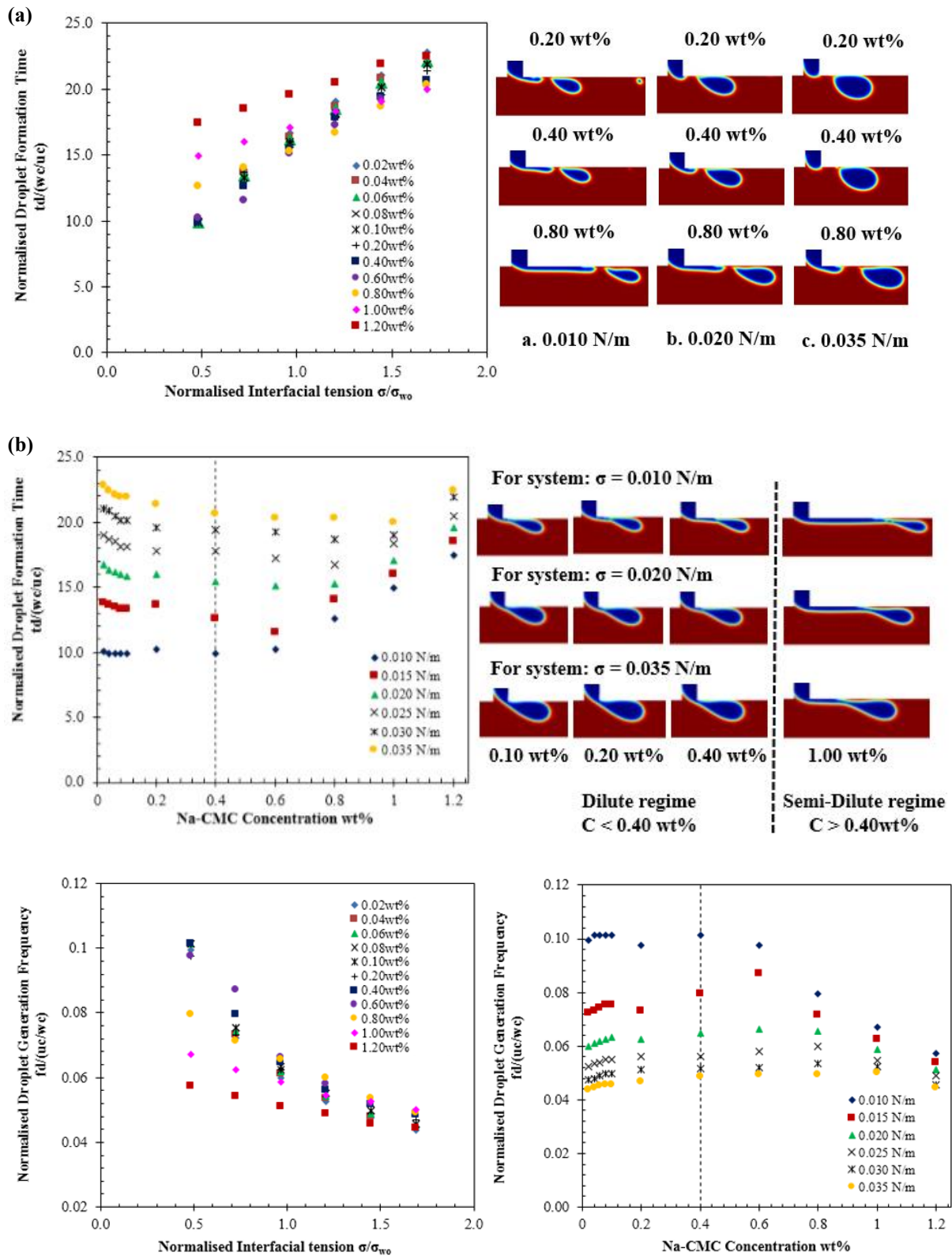
569

570

571

The effect of interfacial tension on the time taken for the droplet growth, deformation and detachment were also investigated. The impact of interfacial tension on the Na-CMC droplet breakup time is illustrated in Fig. 12(a). As a result, the droplet breakup time increases with increasing interfacial tension. As interfacial tension increases, the retraction of the interface induced by surface tension forces becomes greater due to the relatively high surface free energy. This will tend to hinder the droplet formation process as the Na-CMC droplets take longer time approach to thermodynamics equilibrium. At the low concentration regime ($C < 0.40$ wt%), the droplet is pinched-off sharply at the corner of T-junction. In addition, this breakup regime is driven primarily

572 by the build-up of pressure upstream which is mainly due to the high degree of
 573 confinement of the droplet in bulk phase.



574

575
 576

577
 578
 579
 580

Fig. 12: (a) Effect of interfacial tension on the normalized droplet formation time of Na-CMC solutions (for system: $Q_d/Q_c=0.05$). (b) Variation in normalized droplet formation rate of Na-CMC droplets for various concentrations at each interfacial tension (σ).

581 The droplet breakup time decreases when Na-CMC concentration is increased from
582 0.02 wt% to 0.40 wt% (see Figure 12(b)). In contrast to this phenomenon, the break-
583 up time increases as Na-CMC concentration is larger than 0.40 wt%. For dilute Na-
584 CMC concentrations below 0.40 wt%, the interfacial forces are more dominant than
585 viscous forces due to the insufficient polymer chain overlap leading to earlier
586 occurrence of pinch-off. While the Na-CMC concentrations above 0.40 wt%, interfacial
587 forces are less prevalent in strength and the larger viscosities give rise to longer
588 breakup time which can be attributed to the higher magnitude of the dispersed thread
589 pressure. A similar observation has been reported by Zhang and Basaran (1995) who
590 studied the high viscous pendant drops (Zhang & Basaran, 1995). Tirtaatmadja *et al.*
591 (2006) also claimed that the polymer molecules can be highly extended during their
592 approach to pinch region and this contributes to the formation of filament. The filament
593 can be further extended by the stretching force at a constant rate until full extension
594 of polymer coil is achieved (Tirtaatmadja, McKinley, & Cooper-White, 2006). In
595 general, high stretching of polymer chains is associated with high elasticity.

596

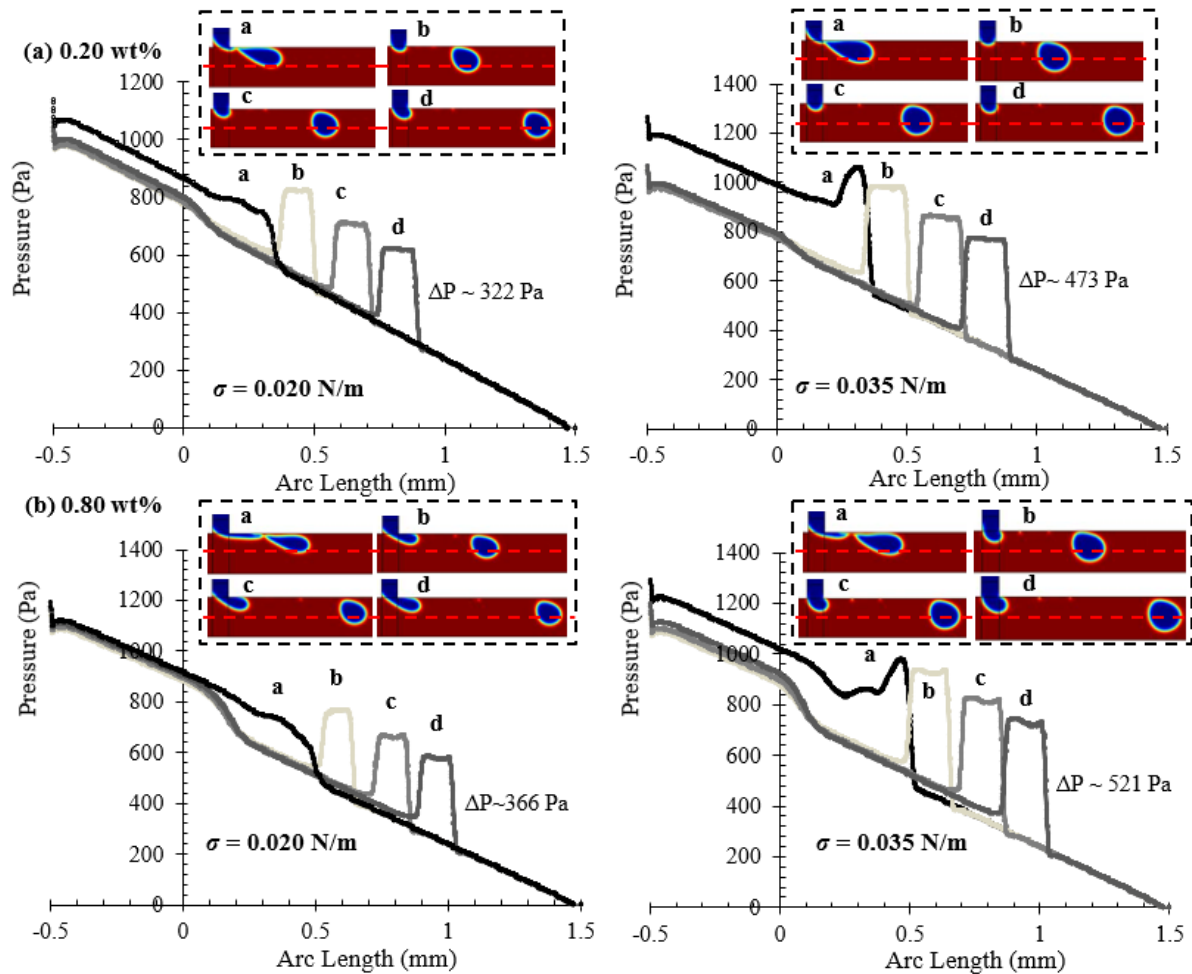
597 For simplicity the viscous force is disregarded, the jetting phenomena and the
598 prolonged thinning of the fluid filament at the rear is more substantial for the shear-
599 thinning droplet with lower interfacial tension at dilute concentration regimes. Less
600 energy is required to disrupt an interface with low magnitude of interfacial tension.
601 Thus, low interfacial tension liquid thread tends to breakup rapidly. Nevertheless, at
602 low Q , jetting occurs when the inertial forces induced by continuous phase exceed
603 interfacial tension forces. As noted in the previous observation, the length of filament
604 gets longer when the Na-CMC polymer concentration is increased. This presumably
605 prevents the neck of the dispersed thread from pinching off. Thus, the existence of a
606 thin polymeric filament will tend to decelerate the breakup process, especially for $C >$
607 0.40 wt%. Previous studies have reported that the formation of filament was due to the
608 elasticity effect. Nevertheless, a similar behaviour was also found for the working
609 solution which is purely viscous and shear-thinning characteristics at the larger
610 concentrations.

611

612 The breakup time for a droplet is increased leading to a decreased production rate at
613 fixed Q for larger magnitude of interfacial tension forces. This exhibits the similar
614 observations to the studies made by Peng *et al.* (2011) and Bashir *et al.* (2011) who

615 studied water-oil emulsions in flow-focusing and cross-flowing microfluidics devices,
616 respectively. The droplet production rate at each fixed interfacial tension has been
617 investigated. In lower concentration regimes ($C < 0.40$ wt%), the earlier occurrence of
618 droplet breakup is observed. In contrast, the production rate decreases with increasing
619 the Na-CMC concentration in the semi-dilute concentration regime ($C > 0.40$ wt%), it
620 takes a longer time for the dispersed phase viscous force to be overcome by the
621 opposing inertial force and shear stress induced by the continuous phase.

622
623 The pressure-jump profiles of Na-CMC droplet at different interfacial tensions were
624 illustrated in Fig. 13. At lower concentration of Na-CMC solutions, the larger interfacial
625 tension contributes to a larger pressure drop profile. As interfacial tension increases,
626 the strength of attractive force increases and causes the liquid surface to contract
627 toward the interior phase and thus the repulsive collisional forces is reduced in order
628 to resist the contraction. Thus, the breakup process of droplet is hindered and larger
629 droplet is generated. Similarly, fluids with the higher concentration produce larger size
630 droplets at the larger surface tensions. Nevertheless, the generation of smaller
631 droplets did not reveal a larger pressure-drop profiles when compare to the previous
632 consequences. It is postulated that the effect of surface tension enables higher surface
633 energy which is caused by the gradient of confinement. Forcing the detached droplet
634 translocate through a confined region will increase the pressure within the droplet at
635 the location where it is almost fully occupied. This causes the increment of the
636 curvature effect that requires the external fluid to apply the extra pressure.



637

638 **Fig. 13:** A qualitative plot of the Laplace pressure profile of a generated Na-CMC
 639 droplet interface curvature at concentration of 0.20 wt% and 0.80 wt% along the middle
 640 plane of microchannel at $\sigma = 130^\circ$ and 170° (for system: $Q_d/Q_c=0.05$).
 641

642

5. Conclusions

643

644 The essential role of viscosity, surface wettability, and interfacial tension on
 645 emulsification process of Na-CMC shear-thinning droplet has been highlighted in the
 646 present simulation using conservative level-set numerical method. The evolution of
 647 the breakup time and the droplet production rate is effectively governed by the physical
 648 properties of working fluid. Olive oil was selected as the continuous phase while the
 649 Na-CMC polymer was used as the non-Newtonian dispersed phase fluid. The present
 650 simulation data revealed that droplet breakup time and production rate have a striking
 651 non-monotonic relationship with the Na-CMC polymer concentration due to the
 652 considerable rheological shear-thinning nature of Na-CMC polymer solution. As the
 653 concentration increases, the polymer concentration crosses over from the dilute to
 semi-dilute regime. While $C < 0.40$ wt%, the droplet breakup time decreases when the

654 Na-CMC concentration is increased at fixed θ and σ . While in semi-dilute regime,
655 droplet breakup time increases when if Na-CMC concentration is increased. This
656 phenomenon is mainly due to the dispersed phase viscous forces dominating over the
657 breakup dynamics and relevant hydrodynamics. As Na-CMC concentration increases,
658 a laminar elongated dispersed thread is formed connecting to the primary droplet due
659 to the high viscous pressure, and thus the droplet breakup point moves progressively
660 downstream of the outlet channel. The presence of high concentration of polymer
661 molecules leads to a prolonged fluid thread and retardation of pinch-off development.
662 In present parametric analysis, there are many features that were previously attributed
663 to elastic effects that still remain a defining challenge for the highly shear-thinning and
664 viscous Na-CMC polymer solution. This illustrates the potential of integrating the
665 elastic stress model with present numerical method, in order to investigate the fluid
666 elasticity effect on the growth of droplet with shear-thinning characteristics.

667

668 **Nomenclature**

669 a Fitting parameter in Carreau-Yasuda model

670 d_{eff} Effective droplet diameter (μm)

671 F_{st} Surface tension force acting on the interface (N/m^3)

672 F_D Cross flow drag force (N/m^3)

673 h Depth of the channel (μm)

674 I Identity matrix

675 k Curvature of fluid-fluid interface

676 n Power-law exponent for Carreau-Yasuda Model

677 \mathbf{n}_r Unit normal vector at the interface

678 p Pressure (N/m^2)

679 Q Flow rate ratio

680 Q_c Flow rate of the continuous phase (ml/hr)

681	Q_d	Flow rate of the dispersed phase (ml/hr)
682	t	Time-step (s)
683	u	Velocity component in x-direction (m/s)
684	v	Velocity component in y-direction (y-direction) (m/s)
685	\mathbf{u}	Velocity field
686	R	Curvature radii of the interface (m)

687

688 **Greek Symbols**

689	η	Dynamic viscosity of fluid (Pa.s)
690	η_d	Dynamic viscosity of the dispersed phase (Pa.s)
691	η_c	Dynamic viscosity of the continuous phase (Pa.s)
692	η_0	Zero shear viscosity (Pa.s)
693	η_∞	Infinite shear viscosity (Pa.s)
694	λ_η	Viscosity ratio (η_d/η_c)
695	λ_{CY}	Relaxation Time in Carreau-Yasuda Model(s)
696	ρ	Fluid density (kg/m ³)
697	τ	Shear stress (Pa)
698	$\dot{\gamma}$	Shear rate (1/s)
699	γ	Reinitialization parameter (m/s)
700	ε	Thickness of the interface (m)
701	σ	Interfacial tension (mN/m)
702	ϕ	Level set function
703	δ_{sm}	Dirac delta function concentrated at interface

704 Ω Computational domain

705 $\partial\Omega$ Domain boundary

706 **Acknowledgement**

707 This research project was financially supported by Malaysia Intercampus Doctoral
708 Award Scheme (MIDAS).

709 **References**

- 710 Anna, S. L., & Mayer, H. C. (2006). Microscale tipstreaming in a microfluidic flow
711 focusing device. *Physics of Fluids*, 18(12), 121512. doi:10.1063/1.2397023
- 712 Arratia, P. E., Cramer, L. A., Gollub, J. P., & Durian, D. J. (2009). The effects of polymer
713 molecular weight on filament thinning and drop breakup in microchannels. *New*
714 *Journal of Physics*, 11(11), 115006.
- 715 Bashir, S., Rees, J.M., Zimmerman, W.B. (2011). Simulations of microfluidics droplet
716 formation using the two-phase level set method. *Chemical Engineering*
717 *Sciences*, 66, 4733-4741.
- 718 Bonometti, T., & Magnaudet, J. (2007). An interface-capturing method for
719 incompressible two-phase flows. Validation and application to bubble
720 dynamics. *International Journal of Multiphase Flow*, 33(2), 109-133.
721 doi:<https://doi.org/10.1016/j.ijmultiphaseflow.2006.07.003>
- 722 Chhabra, R. P., & Richardson, J. F. (2008). Chapter 1 - Non-Newtonian Fluid
723 Behaviour. In R. P. Chhabra & J. F. Richardson (Eds.), *Non-Newtonian Flow*
724 *and Applied Rheology (Second Edition)* (pp. 1-55). Oxford: Butterworth-
725 Heinemann.
- 726 Cramer, C., Fischer, P., & Windhab, E. J. (2004). Drop formation in a co-flowing
727 ambient fluid. *Chemical Engineering Science*, 59(15), 3045-3058.
728 doi:<https://doi.org/10.1016/j.ces.2004.04.006>
- 729 Davidson, M. R., & Cooper-White, J. J. (2006). Pendant drop formation of shear-
730 thinning and yield stress fluids. *Applied Mathematical Modelling*, 30(11), 1392-
731 1405. doi:<https://doi.org/10.1016/j.apm.2006.03.016>
- 732 Davidson, M. R., Cooper-White, J. J., & Tirtaatmadja, V. (2004). Shear-thinning drop
733 formation. *ANZIAM Journal; Vol 45 (2003)*.
- 734 Deshpande, K. B., & Zimmerman, W. B. (2006). Simulation of interfacial mass transfer
735 by droplet dynamics using the level set method. *Chemical Engineering Science*,
736 61(19), 6486-6498. doi:<https://doi.org/10.1016/j.ces.2006.06.012>
- 737 Garstecki, P., Fuerstman, M. J., Stone, H. A., & Whitesides, G. M. (2006). Formation
738 of droplets and bubbles in a microfluidic T-junction-scaling and mechanism of
739 break-up. *Lab on a Chip*, 6(3), 437-446. doi:10.1039/B510841A
- 740 Hong, J. S., & Cooper-White, J. (2009). Drop formation of Carbopol dispersions
741 displaying yield stress, shear thinning and elastic properties in a flow-focusing
742 microfluidic channel. *Korea-Australia Rheology Journal*, 21(4), 269-280.
- 743 Hou, T. Y., Lowengrub, J. S., & Shelley, M. J. (2001). Boundary Integral Methods for
744 Multicomponent Fluids and Multiphase Materials. *Journal of Computational*
745 *Physics*, 169(2), 302-362. doi:<https://doi.org/10.1006/jcph.2000.6626>

746 Huebner, A., Sharma, S., Srisa-Art, M., Hollfelder, F., Edel, J. B., & deMello, A. J.
747 (2008). Microdroplets: A sea of applications? *Lab on a Chip*, 8(8), 1244-1254.
748 doi:10.1039/B806405A

749 Husny, J., & Cooper-White, J. J. (2006). The effect of elasticity on drop creation in T-
750 shaped microchannels. *Journal of Non-Newtonian Fluid Mechanics*, 137(1),
751 121-136. doi:<https://doi.org/10.1016/j.jnnfm.2006.03.007>

752 Kobayashi, I., Nakajima, M., & Mukataka, S. (2003). Preparation characteristics of oil-
753 in-water emulsions using differently charged surfactants in straight-through
754 microchannel emulsification. *Colloids and Surfaces A: Physicochemical and
755 Engineering Aspects*, 229(1), 33-41.
756 doi:<https://doi.org/10.1016/j.colsurfa.2003.08.005>

757 Leshansky, A. M., & Pismen, L. M. (2009). Breakup of drops in a microfluidic T junction.
758 *Physics of Fluids*, 21(2), 023303. doi:10.1063/1.3078515

759 Moon, S.-K., Cheong, I. W., & Choi, S.-W. (2014). Effect of flow rates of the continuous
760 phase on droplet size in dripping and jetting regimes in a simple fluidic device
761 for coaxial flow. *Colloids and Surfaces A: Physicochemical and Engineering
762 Aspects*, 454, 84-88. doi:<https://doi.org/10.1016/j.colsurfa.2014.04.006>

763 Niu, X., & deMello, Andrew J. (2012). Building droplet-based microfluidic systems for
764 biological analysis. *Biochemical Society Transactions*, 40(4), 615.

765 Olsson, E., & Kreiss, G. (2005). A conservative level set method for two phase flow.
766 *Journal of Computational Physics*, 210(1), 225-246.
767 doi:<https://doi.org/10.1016/j.jcp.2005.04.007>

768 Olsson, E., Kreiss, G., & Zahedi, S. (2007). A conservative level set method for two
769 phase flow II. *Journal of Computational Physics*, 225(1), 785-807.
770 doi:<https://doi.org/10.1016/j.jcp.2006.12.027>

771 Osher, S., & Sethian, J. A. (1988). Fronts propagating with curvature-dependent
772 speed: Algorithms based on Hamilton-Jacobi formulations. *Journal of
773 Computational Physics*, 79(1), 12-49. doi:[https://doi.org/10.1016/0021-
774 9991\(88\)90002-2](https://doi.org/10.1016/0021-9991(88)90002-2)

775 Peng, L., Yang, M., Guo, S.-s., Liu, W., & Zhao, X.-z. (2011). The effect of interfacial
776 tension on droplet formation in flow-focusing microfluidic device. *Biomed
777 Microdevices*, 13(3), 559-564. doi:10.1007/s10544-011-9526-6

778 Qiu, D., Silva, L., Tonkovich, A. L., & Arora, R. (2010). Micro-droplet formation in non-
779 Newtonian fluid in a microchannel. *Microfluidics and Nanofluidics*, 8(4), 531-
780 548. doi:10.1007/s10404-009-0487-5

781 Rider, W. J., & Kothe, D. B. (1998). Reconstructing Volume Tracking. *Journal of
782 Computational Physics*, 141(2), 112-152.
783 doi:<https://doi.org/10.1006/jcph.1998.5906>

784 Shui, L., van den Berg, A., & Eijkel, J. C. T. (2009). Interfacial tension controlled W/O
785 and O/W 2-phase flows in microchannel. *Lab on a Chip*, 9(6), 795-801.
786 doi:10.1039/B813724B

787 Steinhaus, B., Shen, A. Q., & Sureshkumar, R. (2007). Dynamics of viscoelastic fluid
788 filaments in microfluidic devices. *Physics of Fluids*, 19(7), 073103.
789 doi:10.1063/1.2747660

790 Takada, N., Misawa, M., Tomiyama, A., & Fujiwara, S. (2000). Numerical simulation of
791 two- and three-dimensional two-phase fluid motion by lattice Boltzmann
792 method. *Computer Physics Communications*, 129(1), 233-246.
793 doi:[https://doi.org/10.1016/S0010-4655\(00\)00110-7](https://doi.org/10.1016/S0010-4655(00)00110-7)

794 Tawfik, D. S., & Griffiths, A. D. (1998). Man-made cell-like compartments for molecular
795 evolution. *Nature Biotechnology*, 16, 652. doi:10.1038/nbt0798-652

796 Theberge Ashleigh , B., Courtois, F., Schaerli, Y., Fischlechner, M., Abell, C.,
797 Hollfelder, F., & Huck Wilhelm , T. S. (2010). Microdroplets in Microfluidics: An
798 Evolving Platform for Discoveries in Chemistry and Biology. *Angewandte*
799 *Chemie International Edition*, 49(34), 5846-5868. doi:10.1002/anie.200906653
800 Thorsen, T., Roberts, R. W., Arnold, F. H., & Quake, S. R. (2001). Dynamic Pattern
801 Formation in a Vesicle-Generating Microfluidic Device. *Physical Review*
802 *Letters*, 86(18), 4163-4166. doi:10.1103/PhysRevLett.86.4163
803 Tirtaatmadja, V., McKinley, G. H., & Cooper-White, J. J. (2006). Drop formation and
804 breakup of low viscosity elastic fluids: Effects of molecular weight and
805 concentration. *Physics of Fluids*, 18(4), 043101. doi:10.1063/1.2190469
806 Tryggvason, G., Bunner, B., Esmaeeli, A., Juric, D., Al-Rawahi, N., Tauber, W., . . . Jan,
807 Y. J. (2001). A Front-Tracking Method for the Computations of Multiphase Flow.
808 *Journal of Computational Physics*, 169(2), 708-759.
809 doi:<https://doi.org/10.1006/jcph.2001.6726>
810 Umbanhowar, P. B., Prasad, V., & Weitz, D. A. (2000). Monodisperse Emulsion
811 Generation via Drop Break Off in a Coflowing Stream. *Langmuir*, 16(2), 347-
812 351. doi:10.1021/la990101e
813 Utada, A. S., Fernandez-Nieves, A., Stone, H. A., & Weitz, D. A. (2007). Dripping to
814 Jetting Transitions in Coflowing Liquid Streams. *Physical Review Letters*, 99(9),
815 094502. doi:10.1103/PhysRevLett.99.094502
816 van der Zwan, E., Schroën, K., & Boom, R. (2009). A Geometric Model for the
817 Dynamics of Microchannel Emulsification. *Langmuir*, 25(13), 7320-7327.
818 doi:10.1021/la900379n
819 Wong, V.-L., Loizou, K., Lau, P.-L., Graham, R. S., & Hewakandamby, B. N. (2017).
820 Numerical studies of shear-thinning droplet formation in a microfluidic T-junction
821 using two-phase level-SET method. *Chemical Engineering Science*, 174, 157-
822 173. doi:<https://doi.org/10.1016/j.ces.2017.08.027>
823 Xu, J. H., Li, S. W., Tan, J., & Luo, G. S. (2008). Correlations of droplet formation in T-
824 junction microfluidic devices: from squeezing to dripping. *Microfluidics and*
825 *Nanofluidics*, 5(6), 711-717. doi:10.1007/s10404-008-0306-4
826 Yobas, L., Martens, S., Ong, W.-L., & Ranganathan, N. (2006). High-performance flow-
827 focusing geometry for spontaneous generation of monodispersed droplets. *Lab*
828 *on a Chip*, 6(8), 1073-1079. doi:10.1039/B602240E
829 Zhang, X., & Basaran, O. A. (1995). An experimental study of dynamics of drop
830 formation. *Physics of Fluids*, 7(6), 1184-1203. doi:10.1063/1.868577
831